Quasi 6-Day Planetary Wave Oscillations in Equatorial Plasma Irregularities

Nicholas Pedatella[1], Ercha Aa[2], and Astrid Maute[3]

[1]High Altitude Observatory, NSF National Center for Atmospheric Research
[2]Haystack Observatory, Massachusetts Institute of Technology
[3]Cooperative Institute for Research in Environmental Sciences, University of Colorado

March 29, 2024

Abstract

The influence of atmospheric planetary waves on the occurrence of irregularities in the low latitude ionosphere is investigated using Whole Atmosphere Community Climate Model with thermosphere-ionosphere eXtension (WACCM-X) simulations and Global Observations of the Limb and Disk (GOLD) observations. GOLD observations of equatorial plasma bubbles (EPBs) exhibit a ~6-8 day periodicity during January-February 2021. Analysis of WACCM-X simulations, which are constrained to reproduce realistic weather variability in the lower atmosphere, reveals that this coincides with an amplification of the westward propagating wavenumber-1 quasi-six day wave (Q6DW) in the mesosphere and lower thermosphere (MLT). The WACCM-X simulated Rayleigh-Taylor (R-T) instability growth rate, considered as a proxy of EPB occurrence, is found to exhibit a ~6-day periodicity that is coincident with the enhanced Q6DW in the MLT. Additional WACCM-X simulations performed with fixed solar and geomagnetic activity demonstrate that the ~6-day periodicity in the R-T instability growth rate is related to the forcing from the lower atmosphere. The simulations suggest that the Q6DW influences the day-to-day formation of EPBs through interaction with the migrating semidiurnal tide. This leads to periodic oscillations in the zonal winds, resulting in periodic variability in the strength of the prereversal enhancement, which influences the R-T instability growth rate and EPBs. The results demonstrate that atmospheric planetary waves, and their interaction with atmospheric tides, can have a significant impact on the day-to-day variability of EPBs.

Quasi 6-Day Planetary Wave Oscillations in Equatorial Plasma Irregularities

N. M. Pedatella[1,2], E. Aa[3], and A. Maute[4]

[1]High Altitude Observatory, NSF National Center for Atmospheric Research, Boulder, CO, USA.
[2]COSMIC Program Office, University Center for Atmospheric Research, Boulder, CO, USA.
[3]Haystack Observatory, Massachusetts Institute of Technology, Westford, MA, USA.
[4]Cooperative Institute for Research in Environmental Sciences, University of Colorado, Boulder, CO, USA.

Key Points:

- A ∼6-day oscillation occurs in observed equatorial plasma bubbles (EPBs) during January 2021.
- Analysis of simulations reveals that the ∼6-day oscillation in EPBs is due to the quasi-six day planetary wave.
- Planetary waves influence EPBs through modulation of the semidiurnal tide and the prereversal enhancement.

Corresponding author: Nicholas Pedatella, `nickp@ucar.edu`

Abstract

The influence of atmospheric planetary waves on the occurrence of irregularities in the low latitude ionosphere is investigated using Whole Atmosphere Community Climate Model with thermosphere-ionosphere eXtension (WACCM-X) simulations and Global Observations of the Limb and Disk (GOLD) observations. GOLD observations of equatorial plasma bubbles (EPBs) exhibit a ∼6-8 day periodicity during January-February 2021. Analysis of WACCM-X simulations, which are constrained to reproduce realistic weather variability in the lower atmosphere, reveals that this coincides with an amplification of the westward propagating wavenumber-1 quasi-six day wave (Q6DW) in the mesosphere and lower thermosphere (MLT). The WACCM-X simulated Rayleigh-Taylor (R-T) instability growth rate, considered as a proxy of EPB occurrence, is found to exhibit a ∼6-day periodicity that is coincident with the enhanced Q6DW in the MLT. Additional WACCM-X simulations performed with fixed solar and geomagnetic activity demonstrate that the ∼6-day periodicity in the R-T instability growth rate is related to the forcing from the lower atmosphere. The simulations suggest that the Q6DW influences the day-to-day formation of EPBs through interaction with the migrating semidiurnal tide. This leads to periodic oscillations in the zonal winds, resulting in periodic variability in the strength of the prereversal enhancement, which influences the R-T instability growth rate and EPBs. The results demonstrate that atmospheric planetary waves, and their interaction with atmospheric tides, can have a significant impact on the day-to-day variability of EPBs.

1 Introduction

Equatorial Plasma Bubbles (EPBs) occur in the post-sunset equatorial and low latitude ionosphere and are an important space weather phenomenon due to their influence on radio wave propagation. EPBs are characterized by regions of low plasma density that extend upwards from the bottomside of the ionospheric F-region, becoming more turbulent at higher altitudes. EPBs arise due to the generalized Rayleigh-Taylor (R-T) instability, which causes the low latitude ionosphere to become unstable under certain conditions. The occurrence of EPBs has been widely studied observationally, theoretically, and with numerical simulations (see reviews by Fejer & Kelley, 1980; Hysell, 2000; Kelley et al., 2011; Yokoyama, 2017; Huba, 2021). These studies have led to a general understanding of the EPB occurrence climatology and the mechanisms controlling the climatological variability. The seasonal and longitudinal variability of EPBs is largely controlled by the angle between the sunset terminator and the magnetic field declination (Tsunoda, 1985; Burke et al., 2004; Gentile et al., 2006). At times when the two are aligned, the E-region conductivity decreases simultaneously in both hemispheres. This leads to an increase in the R-T instability growth rate due to the decrease in field-line integrated E-region conductivity and by enhancing the early evening upward plasma drifts (i.e., prereversal enhancement, PRE) (Fejer et al., 1999).

Although the climatological variability of EPBs can largely be explained by seasonal changes in the alignment of the the solar terminator and magnetic field lines, this does not explain the significant day-to-day variability in observed EPB occurrence. The daily variability in EPB occurrence has yet to be fully explained, but several mechanisms have been proposed to explain the day-to-day variability in EPBs. Proposed mechanisms for driving the day-to-day variability in EPBs include geomagnetic activity (Abdu et al., 2003; Ram et al., 2008; Abdu, Kherani, Batista, & Sobral, 2009; Carter et al., 2014), gravity wave seeding and large-scale wave structures (Makela & Miller, 2008; Abdu, Kherani, Batista, de Paula, et al., 2009; Huba & Liu, 2020), F-region neutral winds (Abdu, Iyer, et al., 2006; Huba & Krall, 2013), sporadic E-layers (Stephan et al., 2002; Tsunoda, 2007; Huba et al., 2020), and the PRE (Fejer et al., 1999; Carter et al., 2014; Aa et al., 2023).

Note that these mechanisms are not mutually exclusive, and several different mechanisms may be simultaneously driving the EPB day-to-day variability.

The PRE is an important factor in controlling the occurrence of EPBs. In particular, the large upward plasma drifts associated with a strong PRE enhance the R-T instability growth rate leading to preferential conditions for the formation of EPBs. In contrast, downward (or weakly upward) drifts are stabilizing and are associated with the absence of EPBs (Fejer et al., 1999; Su et al., 2008; Kil et al., 2009; Huang & Hairston, 2015). Variability in the PRE is thus an important factor controlling the day-to-day occurrence of EPBs. On seasonal time scales, the PRE is determined by the alignment of the solar terminator with the magnetic declination, which influences the relative importance of the E- and F-region dynamos and in-turn the strength of the polarization electric fields at the terminator. The strength of the PRE is also determined by the neutral winds in the E- and F-regions. The contribution of the E- and F-region winds to the PRE is complex, potentially varying with season and time-scale. The F-region winds appear to be more important during equinox and on seasonal time scales, while the contribution from E-region winds is potentially more important during solstice and on day-to-day time scales (Richmond et al., 2015; Liu, 2020). The neutral winds at E-region altitudes are strongly influenced by atmospheric tides, and the amplitude and phase of the tides can significantly impact the strength of the PRE, including its day-to-day variability (Liu, 2020; Ghosh et al., 2020; Yamazaki & Diéval, 2021).

Of relevance to the present study is the connection between atmospheric tides and planetary waves, and how they may influence the occurrence of EPBs through modulating the strength of the PRE. Because planetary waves dissipate below ∼100 km, the interaction between planetary waves and tides is considered the primary pathway by which planetary waves impact the ionosphere-thermosphere. Planetary waves act to modulate the spectrum of atmospheric tides in the mesosphere and thermosphere through two main mechanisms. First, the influence of planetary waves on the background tidal propagation conditions can lead to the tidal amplitude varying at planetary wave periods (e.g., Pancheva et al., 2002; Forbes, Zhang, et al., 2018). For example, Pancheva et al. (2003) observed ∼7 day oscillations in the semidiurnal tide amplitude concurrent with the occurrence of a 6-7 day planetary wave. Second, the nonlinear interaction between tides and planetary waves generates secondary waves that can propagate into the ionosphere-thermosphere (Teitelbaum & Vial, 1991; Liu et al., 2010; Pedatella et al., 2012). Observational and modeling studies have shown that the modulation of the tidal spectrum by planetary waves can significantly influence the day-to-day variability in ionosphere electron densities and electric fields (including the PRE) as well as thermosphere density and composition (Gasperini et al., 2015; Yue et al., 2016; Gan et al., 2017; Gu et al., 2018; Forbes et al., 2021; Miyoshi & Yamazaki, 2020; Yamazaki & Diéval, 2021). These impacts may result in planetary wave periodicities in the occurrence of EPBs (Abdu, Ramkumar, et al., 2006; Abdu, Batista, et al., 2006; Abdu et al., 2015; Aa et al., 2023)

Recently, the National Aeronautics and Space Administration (NASA) Global-scale Observations of the Limb and Disk (GOLD) ultraviolet imager has led to new understanding of how EPBs vary over the American-Atlantic longitude sector. The GOLD observations have revealed that EPBs vary significantly over a wide longitudinal region from one day to the next. This includes notable day-to-day changes in the occurrence (or absence) of EPBs, the EPB longitudinal spacing, and the width of the EPBs (Eastes et al., 2019; Aa et al., 2020; Karan et al., 2020; Martinis et al., 2021; Karan et al., 2023). Multi-day periodic behavior of EPBs has also been observed by GOLD, which was attributed to the influence of atmospheric planetary waves modulating the E-region dynamo (Aa et al., 2023).

The objective of the present study is to use a whole atmosphere model to investigate the role of planetary waves on inducing day-to-day, periodic, variability in the occurrence of EPBs. We focus on the 2020-2021 Northern Hemisphere winter time period, when a quasi-six day oscillation in EPBs was observed by GOLD. Whole Atmosphere Community Climate Model with thermosphere-ionosphere eXtension (WACCM-X) simulations are used to investigate the connection between the quasi-six day planetary wave (Q6DW) activity in the middle atmosphere and day-to-day variations in the R-T growth rate, which is used as a proxy for EPB occurrence. The results demonstrate the important role that lower atmospheric processes play in controlling the day-to-day variability of EPBs, as well as the potential capabilities of whole atmosphere models for understanding the day-to-day variations in EPB occurrence rates.

2 WACCM-X Simulations

WACCM-X is a whole atmosphere chemistry climate model that extends from the surface to the upper thermosphere (4.1×10^{-10} hpa). As described in Liu et al. (2018), WACCM-X incorporates a comprehensive treatment of chemistry, electrodynamics, physics, and thermodynamics to simulate the whole atmosphere from the troposphere to the thermosphere-ionosphere. The model horizontal resolution is 1.9° in latitude and 2.5° in longitude, and the vertical resolution is ∼1-3 km in the troposphere-stratosphere and 0.25 scale heights above 0.96 hPa. To isolate different drivers of the ionosphere-thermosphere variability during the 2020-2021 Northern Hemisphere winter, we perform three different simulations. The first simulation aims to capture the realistic ionosphere-thermosphere variability due to the combination of lower atmosphere and solar/geomagnetic forcing. This simulations uses the specified dynamics mechanism (Smith et al., 2017) to constrain the model meteorology up to ∼50 km to the National Aeronautics and Space Administration NASA Modern-Era Retrospective analysis for Research and Applications version 2 (MERRA-2) (Gelaro et al., 2017). Realistic, time-varying, solar and geomagnetic variability are incorporated through the F10.7 cm solar radio flux and K_p geomagnetic index, respectively. The F10.7 cm solar radio flux is used to parameterize the solar irradiance (Solomon & Qian, 2005) and K_p is used for parameterizing the high-latitude electric potential and auroral precipitation (Heelis et al., 1982; Emery et al., 2012). The second simulation aims to isolate forcing from the lower atmosphere. This simulation constrains the troposphere-stratosphere to MERRA-2, but the F10.7 and K_p are held constant at 75 sfu (1 sfu = $10^{-22}\mathrm{Wm}^{-2}\mathrm{Hz}^{-1}$) and 0^{+}, respectively. The third simulation consists of a 20-member ensemble of free-running (i.e., not constrained to MERRA-2) WACCM-X with realistic solar and geomagnetic activity. The analysis of the S/G Only case is performed by taking the ensemble average and performing all subsequent analysis on the ensemble average. This effectively removes the day-to-day variability of the lower atmosphere, isolating the ionosphere-thermosphere variability due to solar and geomagnetic forcing. Throughout the following we refer to the above mentioned first, second, and third simulations as LA+S/G (Lower Atmosphere + Solar/Geomagnetic), LA Only, and S/G Only, respectively.

WACCM-X does not simulate the formation of EPBs, and we therefore use the generalized R-T instability growth rate as a proxy for the occurrence of EPBs (Sultan, 1996). The R-T instability growth rate is given by

$$\gamma_{RT} = \frac{\Sigma_P^F}{\Sigma_P^E + \Sigma_P^F}\left(V_p - U_L^P - \frac{g_e}{\nu_{eff}}\right)K^F - R_T \tag{1}$$

where Σ_P^E and Σ_P^F are the flux-tube integrated E- and F-region Pedersen conductivities, V_p is the upward plasma drift velocity, U_L^P is the neutral wind perpendicular to the magnetic field in the magnetic meridian plane weighted by the Pedersen conductivity, g_e is the gravitational acceleration, ν_{eff} is the flux-tube integrated effective ion-neutral collision frequency weighted by the electron density, K^F is the vertical gradient of the flux-tube integrated F-region electron density, and R_T is the recombination rate. As in Carter et al. (2014) and Q. Wu (2015), we set the recombination rate equal to zero. An altitude of 150 km is used as the boundary of the E- and F-regions. Throughout the following, we take the maximum value of γ_{RT} between 18-22 local time (LT) at an altitude of 300 km, which corresponds to an altitude near the maximum of γ_{RT}. The seasonal variation of the R-T growth rate in the three WACCM-X simulations is shown in Figures 1a-c. Although there are differences in the day-to-day variability, the general seasonal and longitudinal variability is the same among the three simulations, and matches the observed climatology of EPB occurrence rates (e.g., Gentile et al., 2006). The R-T instability growth rates in WACCM-X are therefore considered to be a reliable proxy for the EPB occurrence rates.

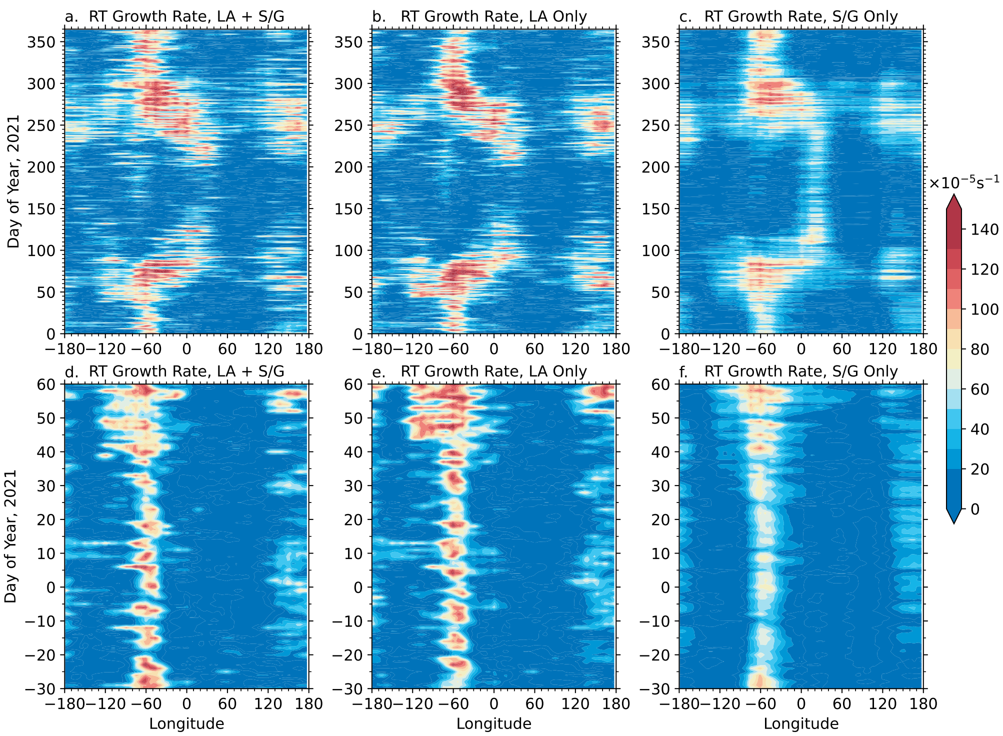

Figure 1. WACCM-X R-T instability growth rate during from January to December 2021 for (a) LA+S/G, (b) LA Only, and (c) S/G Only simulations. (d-f) Same as (a-c) except for the time period of November 2020 to March 2021.

3 GOLD Observations

GOLD is an ultraviolet imaging spectrograph observing the 133-163 nm wavelength range that is hosted onboard the SES-14 geostationary communications satellite (Eastes et al., 2017, 2020; McClintock et al., 2020). During nighttime, GOLD observations of the OI 135.6-nm emission provide information on the structure of the equatorial ionosphere, including the presence of EPBs. To quantify the EPBs observed by GOLD, we use the Bubble Index derived in Aa et al. (2023). Briefly, the Bubble Index is based on calculating the standard deviation of the normalized residual radiance at 135.6-nm, and provides a quantification of the strength of EPBs on any given night within the GOLD field-of-view (~120°W-20°E). As shown in Aa et al. (2023), the GOLD Bubble Index can quantify the day-to-day, seasonal, and solar cycle variation in EPBs.

4 Results and Discussion

Analysis of the GOLD Bubble Index in Aa et al. (2023) revealed the occurrence of periodic variations in EPBs during early 2021, including quasi-six day oscillations in January and February. To understand if this variability could be driven by enhanced planetary wave activity, we first consider the variability in the middle atmosphere during the 2020-2021 Northern Hemisphere winter. Figures 2a and 2c show the period-wavenumber spectra of the WACCM-X temperature and zonal winds during January-February 2021. The results are shown at 0.001 hPa ($\sim$95 km) and at 60°S for temperature and the equator for the zonal wind. These locations correspond to where the Q6DW is expected to obtain large amplitudes (e.g., Gan et al., 2018). The temperature and zonal wind spectra both have a prominent peak at a period of 6-7 days with a westward (positive) wavenumber 1. This indicates the presence of a westward propagating Q6DW with zonal wavenumber 1 (Q6DW W1) during early 2021. The Q6DW W1 is a commonly occurring planetary wave in the MLT, and is thought to be due to doppler shifting of the Rossby normal mode with 5-day period and/or wave amplification related to the background winds (D. L. Wu et al., 1994; Meyer & Forbes, 1997; Talaat et al., 2002; Lieberman et al., 2003; Liu et al., 2004). The temporal variability of the Q6DW W1 amplitude is shown in Figures 2b and 2d for temperature and zonal wind, respectively. The amplitude was obtained by fitting the temperature or zonal wind to a westward propagating wave with zonal wavenumber-1 and a period of 6.7 days in a moving 19-day window. The Q6DW W1 exhibits several small enhancements in November-December 2020 followed by a large amplification beginning in middle to late December 2020 and persisting until late January 2021. The maximum amplitude of the simulated Q6DW in WACCM-X is $\sim$7 K in temperature and $\sim$16 m/s in zonal wind at these locations, which is consistent with typical Q6DW amplitudes seen in observations (Gan et al., 2018).

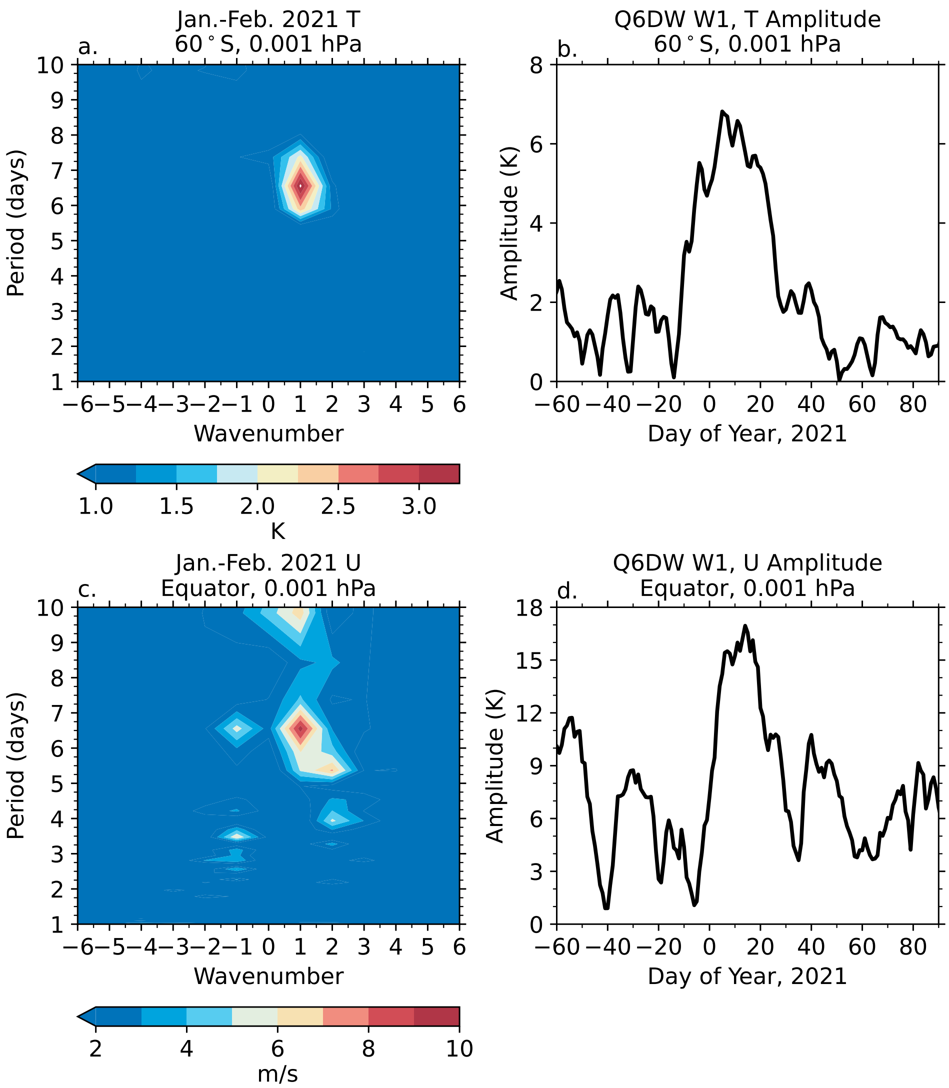

Figure 2. (a) Period-wavenumber spectrum of the WACCM-X temperature at 60°S and 0.001 hPa (∼95 km) during January-February 2021. (b) Amplitude of the westward propagating quasi-six day wave with zonal wavenumber-1 from November 2020 to March 2021. (c-d) Same as (a-b) except the results are for zonal wind at the equator and 0.001 hPa. Results are from the LA+S/G WACCM-X simulation.

Figures 1d-f show the R-T instability growth rate simulated by WACCM-X from December 2020 to February 2021. In all three cases, the R-T instability growth rate maximizes around the American longitude sector, consistent with the seasonal-longitudinal variability of EPBs (e.g., Gentile et al., 2006). Significant day-to-day variability is also evident. Comparison of the R-T instability growth rate among the three different simulations reveals that much of the day-to-day variability that is seen in the LA+S/G simulation also appears in the LA Only simulation, indicating that the day-to-day variability in the R-T instability growth rate is primarily driven by lower atmospheric processes during this time period. The solar and geomagnetic variability does introduce some day-to-day variability; however, it tends to be less prominent compared to the day-to-day variability driven by the lower atmosphere. It is also apparent in Figure 1 that the R-T instability growth rates tend to be slightly larger in the LA+S/G and LA Only cases compared to the S/G Only case. This is due to weaker values of the PRE in the S/G Only case (not shown). We attribute this to the S/G Only case being the ensemble average, which will tend to result in less extreme values of the daily PRE.

The results in Figures 1d-f show quasi-periodic behavior of the R-T instability growth rate during the 2020-2021 Northern Hemisphere winter. To illustrate the dominant periodicities, Figure 3 shows the wavelet power spectra of the R-T instability growth rate for the three WACCM-X simulations. The wavelet power spectra are based on the R-T instability growth rate averaged between 20-120°W geographic longitude, which corresponds roughly to the GOLD field of view as well as the longitude of maximum R-T instability growth rate and EPB occurrence during Northern Hemisphere winter. The wavelet power spectrum of the GOLD Bubble Index is also shown in Figure 3a. The wavelet power spectra for the GOLD Bubble Index and the R-T instability growth rate in the WACCM-X LA+S/G case exhibit some similarities in terms of the timing of the dominant spectral peaks. However, the periodicities tend to be slightly different in the observations and simulations. For example, both have spectral peaks in middle-late January (days 15-25), though the dominant periodicity occurs around 3-days and 8-days in the GOLD observations compared to near 6-days in the WACCM-X LA+S/G simulation. Differences between the two may arise for several reasons. First, the GOLD Bubble Index represents the intensity and occurrence of the observed EPBs while the R-T instability growth rate only indicates if the large-scale conditions are favorable for development of EPBs. The two may thus not be directly comparable. Second, capturing the full extent of the spatial-temporal variability of the whole atmosphere remains challenging, and the WACCM-X simulations may thus not reproduce the spatial-temporal variability with sufficient accuracy to match the true state of the atmosphere. Nonetheless, we are encouraged by the broad similarities between the GOLD observations and WACCM-X simulations, which indicates that the WACCM-X simulation can capture aspects of the observed periodic behavior of the EPBs during the 2020-2021 Northern Hemisphere winter months.

Considering the results of the WACCM-X cases, it is apparent that there are both similarities and differences between the LA+S/G case and the LA Only and S/G Only cases. This indicates that both the lower atmosphere and solar and geomagnetic activity contribute to the periodic variability in the R-T instability growth rate during the 2020-2021 Northern Hemisphere winter time period. We will first discuss the isolated forcing cases, followed by discussion of how the different forcings combine to generate the variability in the LA+S/G case. In the LA Only case, there are spectral peaks around 6-days in mid-December and January. These coincide with amplifications of the Q6DW in the MLT (Figure 2b), which has a large amplification in January with weaker enhancements during December. This suggests that the Q6DW in the MLT is the source of the ∼6-day spectral peaks in the R-T instability growth rate. Details of the mechanism by which the Q6DW may influence the R-T instability growth rate will be discussed later. Additional shorter-period spectral peaks are seen at a period of ∼3-days in early and mid-February. The ∼3-day spectral peaks are likely related to the quasi-three day planetary wave as discussed in Aa et al. (2023). The S/G Only case exhibits spectral peaks around 4-8 days multiple times in January and February, with maxima around day of year 10, 25, and 40-45. A weak enhancement is also apparent in late December (day -10). Shorter period spectral peaks are also evident in middle-late February (days 40-60). In the LA+S/G case, there are notable spectral peaks around 4-8 days in late December (days -15-0) and mid-January (days 15-20), as well as a spectral peak at 8-10 days in mid-February (days 35-55). We note that although these spectral peaks occur at roughly similar timing as those in the LA Only and S/G Only cases, the LA+S/G case is not simply the combination of the individual forcings. The interaction between the two forcings therefore is complex, leading to shifts in both the dominant wave period and timing of the spectral peaks. This is likely the result of the two forcings combining constructively or destructively at different time periods. The LA+S/G case also exhibits spectral peaks at shorter-periods (∼3-day periods) in early January (days 5-10) and mid-February (days 40-45). The later enhancement may be attributed to the aforementioned quasi-three day planetary wave combined with periodic solar and geomagnetic forcing. The source of the ∼3-day spectral peak in early January is less clear as it is not evident in either the LA Only or S/G Only cases. This illustrates that complex interactions can lead to periodicities not present in either lower atmosphere or solar and geomagnetic forcing. For example, the interaction of two periodicities with different phases could give rise to oscillations at a period different than the two original periodicities.

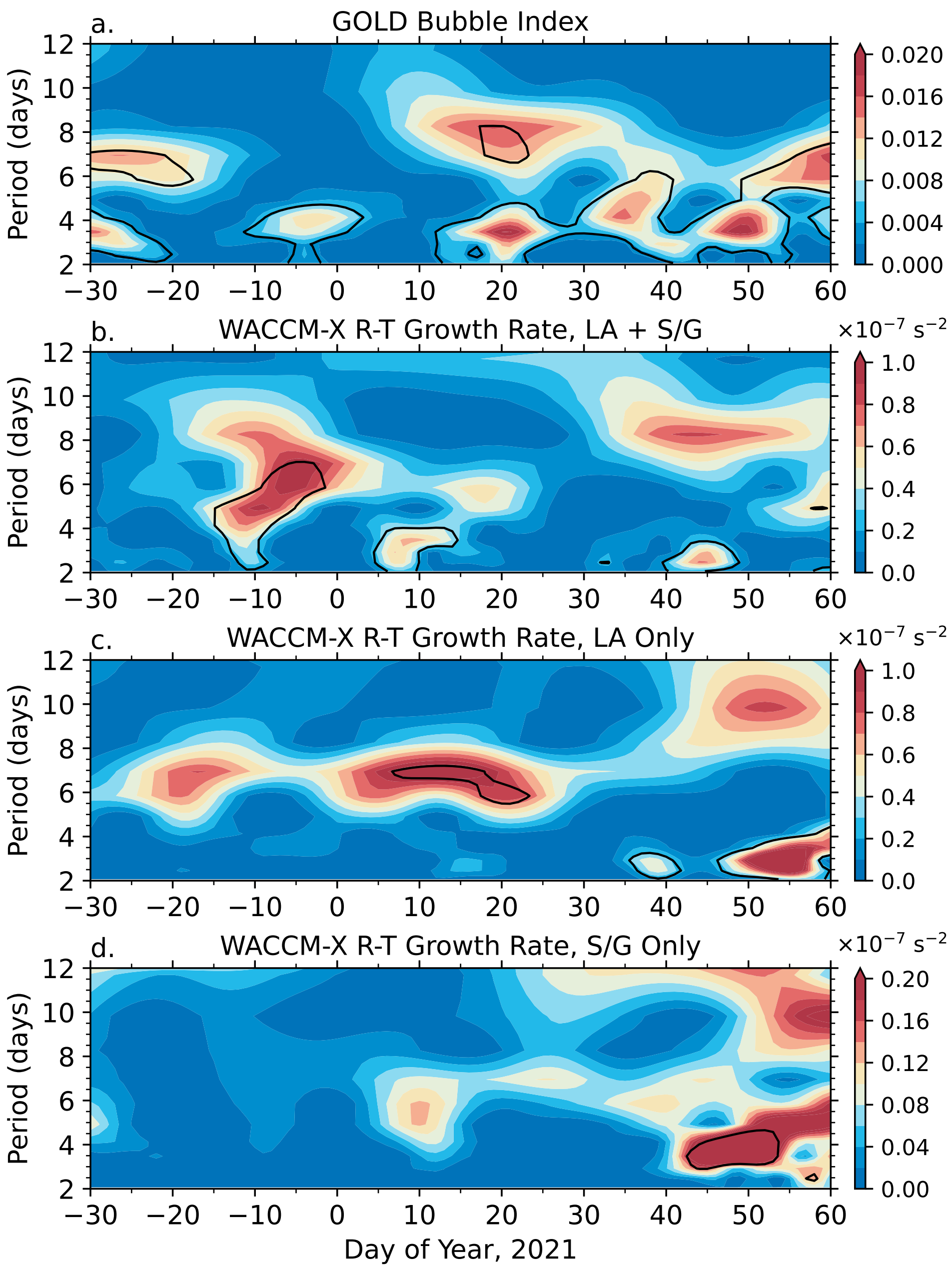

Figure 3. Wavelet analysis of the (a) GOLD Bubble Index and WACCM-X R-T instability growth rate for the (b) LA+S/G, (c) LA only, and (d) S/G only simulations. WACCM-X results are based on the daily mean value of the R-T instability growth rate between 20-120°W geographic longitude. The black contour indicates the 90% significance level.

We now turn our attention to understanding the source of the periodic variations in the R-T instability growth rates. The PRE is considered as on of the primary drivers of the variations in the R-T instability growth rates, and we thus examine the variability in the post-sunset vertical plasma drift velocities. Figure 4a shows the WACCM-X equatorial vertical plasma drift velocity perturbations at 19 local time (LT) for the LA Only case. The Q6DW W1 component of the equatorial vertical plasma drift velocity perturbations is shown in Figure 4b. Note that 19 LT is selected as this corresponds to approximately the time of the PRE in the WACCM-X simulations, and the vertical drift velocity at 19 LT are well correlated with the PRE. The perturbations are obtained by removing a 19-day running mean at each longitude. The Q6DW W1 component is based on fitting the perturbations to a westward propagating wave with a zonal wavenumber-1 and a period of 6.7 days in a moving 19-day window and then reconstructing the longitude-time variations based on the amplitude and phase of the Q6DW W1. Lines corresponding to when the Q6DW W1 obtains maximum and minimum values are included as reference. The results in Figure 4b reveal that there are two time periods of enhanced Q6DW W1 in the equatorial vertical plasma drift velocity. The first time period is in early to mid-December (days -30 to -10) and the second time period is from early January to early February (days 0 to 35). Evidence of the Q6DW W1 structure can be seen in the equatorial vertical plasma drift perturbations (Figure 4a) during these time periods. There are, however, additional sources of variability present in the equatorial vertical plasma drift perturbations, indicating that the Q6DW W1 is not the sole factor driving the variability. We note that the time periods when the Q6DW W1 component of the equatorial vertical drift at 19 LT is enhanced correspond to the times when there is enhanced ∼6-day variability in the R-T instability growth rates (Figure 3c). This demonstrates that the ∼6-day variability in the R-T instability growth rates are most likely driven by the Q6DW W1 variations in the PRE.

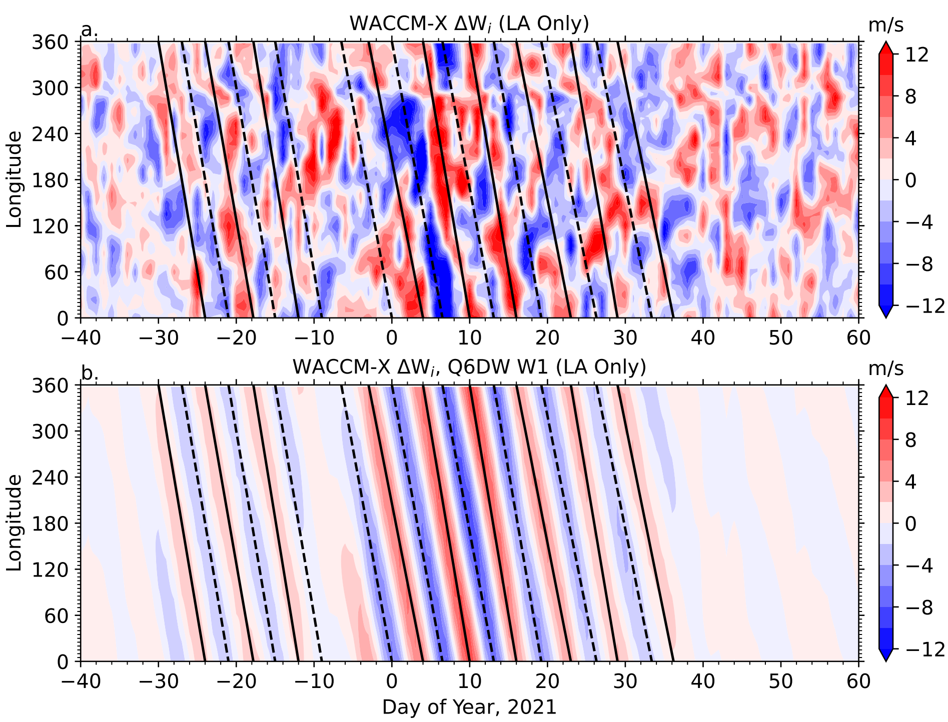

Figure 4. (a) WACCM-X simulated vertical plasma drift velocity residuals at the magnetic equator and 19 local time (LT). (b) Westward propagating quasi six-day wave with zonal wavenumber 1 component of the vertical plasma drift velocity. Results are from the LA Only WACCM-X simulation.

Figure 5a shows the wavelet spectrum of the PRE at the magnetic equator averaged between 20-120°W geographic longitude. The maximum vertical plasma drift velocity between 17-21 LT at each longitude is taken as the PRE velocity at that longitude. The results in Figure 5a are based on calculating the average PRE velocity between 20-120°W for each day. Note that we focus our attention on the results from the LA Only case as we are primarily interested in the role of the Q6DW on introducing periodic variability in the PRE. The results in Figure 5a reveal that the PRE has a dominate spectral peak around 6-days that extends from mid-December 2020 to mid-January 2021. This enhancement is coincident with the occurrence of the ∼6-day spectral peaks in the R-T instability growth rate (Figure 3c) as well as the amplification of the Q6DW in the MLT. We therefore conclude that the ∼6-day periodicity in the R-T instability growth rate during the 2020-2021 Northern Hemisphere winter is primarily driven by periodic variations in the PRE. The results in Figure 5a also show a spectral peak in late February 2021 near ∼3-days, which is consistent with the ∼3-day spectral peak in the R-T instability growth rate, and confirms the results of Aa et al. (2023) that a 3-day planetary wave in February 2021 led to 3-day oscillations in the PRE and EPBs. Although the PRE and R-T instability growth rate wavelet spectra are generally similar, they do exhibit some differences, indicating that factors other than the PRE contribute to the periodic variability in the R-T instability growth rates.

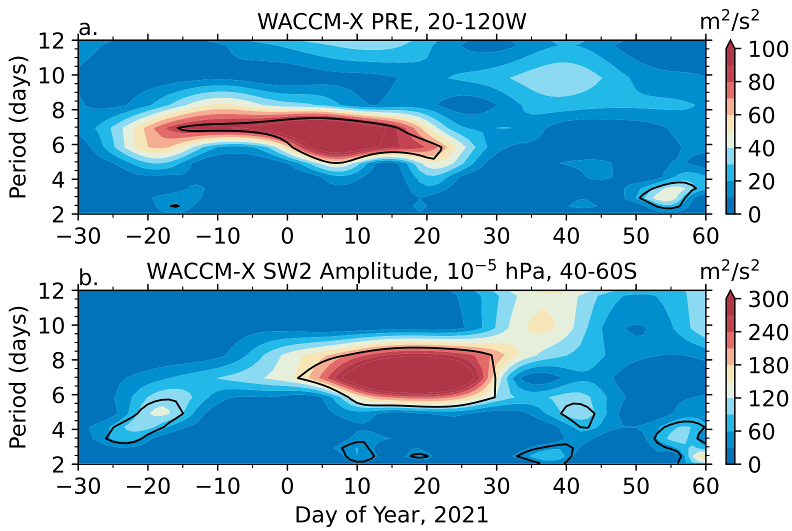

Figure 5. Wavelet analysis of the (a) pre-reversal enhancement vertical drift velocity at the magnetic equator averaged between 20-120°W geographic longitude, and (b) migrating semidiurnal tide (SW2) amplitude in zonal wind at 10^{-5} hPa averaged between 40-60°S. Results are for the LA Only simulation. The black contour indicates the 90% significance level.

The day-to-day variability in the PRE around solstice is significantly influenced by the E-region winds, especially the winds at middle latitudes in the summer hemisphere (e.g., Liu, 2020). Figure 6 shows the normalized daily values of the R-T instability growth rate, PRE, and the zonal wind multiplied by the Pederson conductivity (U$\times\sigma_p$) at 10^{-5} hPa between 30-60°S. The normalization is based on removing the mean and dividing by the standard deviation for each parameter during the time period shown. The results are shown for 300°E geographic longitude. In all three simulation cases, the day-to-day variations in the PRE are similar to the R-T instability growth rates. However, it is also evident that the day-to-day variations in the PRE do not directly map to variations in the R-T instability growth rates, indicating that other factors also contribute to the day-to-day variability in the R-T instability growth rates. This is consistent with previous results that have found generally good agreement between the PRE and R-T instability growth rates (or EPB occurrence rate), but that a large PRE alone does not necessarily mean large R-T instability growth rates or occurrence of EPBs (Kil et al., 2009; Carter et al., 2014). Consistent with Liu (2020), the results in Figure 6 also show that the day-to-day variability in U$\times\sigma_p$ at middle latitudes can be a source of day-to-day variations in the PRE. However, it is again evident that other factors also contribute to the day-to-day variability in the PRE, which may be expected since winds from a wide range of locations can influence the PRE (Liu & Richmond, 2013; Richmond et al., 2015; Liu, 2020). Nonetheless, the results in Figure 6 do indicate the connection between the middle latitude winds, PRE, and R-T instability growth rates on day-to-day time scales.

The results in Figure 6 also show how the planetary wave driven quasi-six day oscillations in the LA Only simulation are modified by the inclusion of the solar and geomagnetic activity. In Figure 6b, quasi-six day variations in U$\times\sigma_p$, PRE, and R-T instability growth rate can be seen beginning in the middle of December and extending until middle January. Although day-to-day variations occur, the quasi-six day variations are absent in the S/G Only case (Figure 6c). The quasi-six day variations can also be seen in the LA+S/G case (Figure 6); however, there is clearly additional variability beyond what is present in the LA Only case. The implications of the solar and geomagnetic variability on understanding sources of the quasi-periodic variations can be seen in a comparison between the R-T instability growth rates during days ∼0-30 in the LA Only and LA+S/G cases. In the LA Only case, there is a clear ∼6-day oscillation during this time period. However, the inclusion of solar and geomagnetic activity distorts this periodic variability, resulting in a ∼3-4 day oscillation around days 5-15. This is despite the fact that there is not a strong 3-4 periodicity in the R-T instability growth rates in the S/G Only simulation. This illustrates the complexity of the interactions between the lower atmosphere and solar/geomagnetic forcing, especially with regards to interpretation of sources of periodic variability.

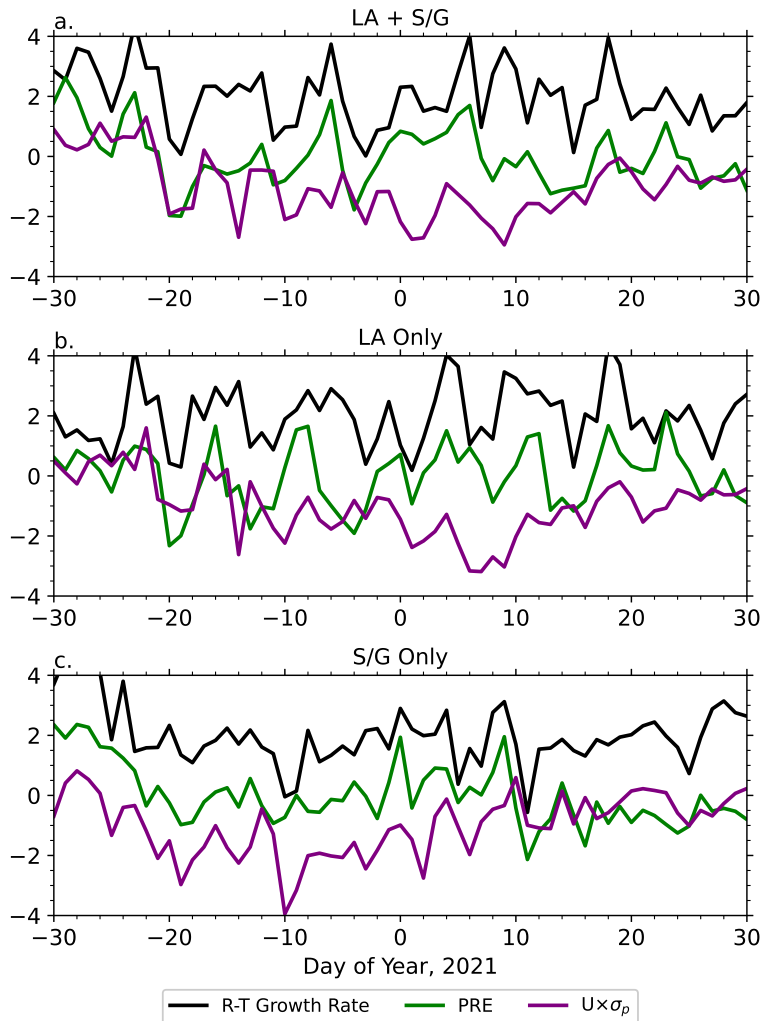

Figure 6. Normalized time series of the zonal wind multiplied by the Pederson conductivity (U×σ_p, purple) at 10^{-5} hPa between 30-60°S, PRE (green), and R-T instability growth rate (black) in WACCM-X for the (a) LA+S/G, (b) LA Only, and (c) S/G Only cases. The R-T instability growth rate is offset by +2.0 and U×σ_p is offset by -1.0

A remaining question is what causes the variations in the middle latitude winds and the PRE. Due to the migrating semidiurnal tide (SW2) obtaining large amplitudes at middle altitudes as well as having significant influence on the PRE (Fesen et al., 2000), we consider variability in the SW2 to be a likely source of the periodic variations in the winds and PRE. Figure 5b shows the wavelet spectrum of the migrating semidiurnal tide (SW2) in zonal wind at 10^{-5} hPa (∼135 km) averaged between 40-60°S. The SW2 has dominant spectral peaks near 6-days around mid-December 2020 and during January 2021. The timing of these enhancements is consistent with the enhanced Q6DW in the MLT as well as the spectral peaks at ∼6-days in the PRE and R-T instability growth rate. The ∼6-day variation in SW2 in mid-December corresponds to a weak Q6DW W1, which may indicate that even relatively weak planetary wave activity can modulate the tidal spectrum. Additional evidence for interactions between the Q6DW and SW2 is shown in Figure 7, which shows the spectra of the zonal wind at 10^{-5} hPa and 45°S for the month of January 2021 for westward propagating wavenumbers 1 and 3. Nonlinear interactions between the Q6DW with 6.5 day period and SW2 are expected to generate secondary waves with periods of 13.0 and 11.1 and zonal wavenumber of 1 and 3, respectively (e.g., Teitelbaum & Vial, 1991). Figure 7a shows a clear spectral peak at a period of 13.0 h and westward wavenumber 1. A less pronounced spectral peak is also evident near 11.1 h for westward wavenumber 3 (Figure 7b). The results in Figure 7 thus indicate the presence of secondary waves arising from the nonlinear interaction between the Q6DW and SW2. Based on these results, we conclude that the Q6DW modulates the amplitude of the SW2 and that the Q6DW and SW2 interact nonlinearly, giving rise to secondary waves. The tidal variations lead to periodic quasi-six day variability in the middle latitude winds, which, in-turn, generate quasi-six day variations in the PRE. This mechanism is consistent with recent modeling results by Forbes, Maute, et al. (2018), who showed that the planetary wave modulation of tides is an important source of variability in equatorial vertical plasma drifts and F-region electron density. As factors other than the middle latitude SW2 can contribute to the PRE variability, there are some differences between the periodic variations in the SW2 and PRE in Figure 5. However, we hypothesize that the SW2 variations are a source of the variations in the PRE. The ~6-day oscillations in the PRE then lead to the ~6-day oscillations in the R-T instability growth rate as well as EPBs.

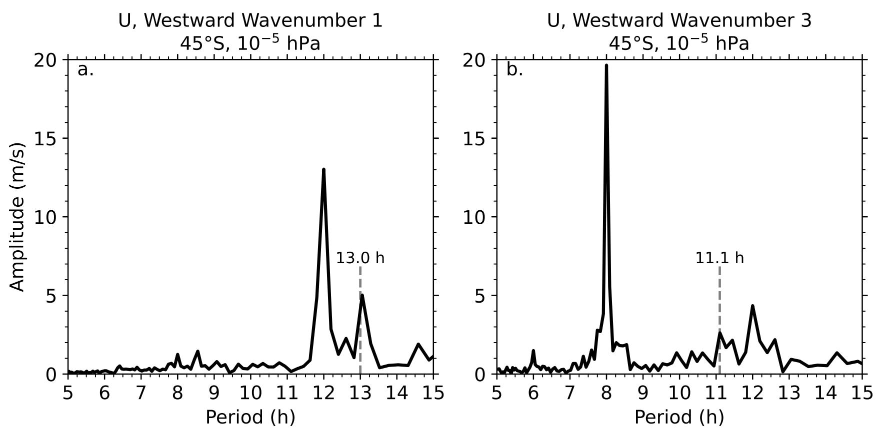

Figure 7. Spectral analysis of the zonal winds at 10^{-5} hPa and 45°S during January 2021 for (a) westward propagating wavenumber 1 and (b) westward propagating wavenumber 3. Results are for the LA Only simulation.

5 Summary and Conclusions

In the present study, we have investigated the influence of atmospheric planetary waves on the day-to-day variability of EPBs. WACCM-X simulations demonstrate that the Q6DW can induce periodic oscillations in the strength of the R-T instability growth rate. Since the R-T instability growth rate is related to the formation of EPBs, we thus conclude that the Q6DW can lead to day-to-day variability in the occurrence and strength of EPBs. This is confirmed by the presence of oscillations at a period of ~6-days in GOLD observations of EPBs during early 2021, coincident with an enhancement in the Q6DW. Analysis of the WACCM-X simulations indicates that the Q6DW impacts the formation of EPBs through a multi-step process. First, the planetary wave interacts with the SW2, leading to a ~6-day oscillation in the SW2 amplitude as well as the generation of secondary waves. Second, the planetary wave modulated tides influence the winds driving the E-region dynamo. This results in periodic variations in the PRE. Last, the variations in the PRE induce the variations with a period of ~6-days in the R-T instability growth rate and EPBs. This chain of events appears to be the primary mechanism by which the Q6DW impacts the day-to-day variability of EPBs, though there may be additional mechanisms given that there is not a one-to-one correspondence between the variations in the SW2, PRE, and R-T instability growth rate.

The results of the present study provide insight into the mechanisms driving the day-to-day variability of EPBs. In particular, it is demonstrated that atmospheric planetary waves can be an important factor in driving the day-to-day variability in the formation of EPBs. Planetary waves may have additional impacts on the formation of EPBs beyond what is discussed in the present study. For example, the filtering of gravity waves by planetary waves (Smith, 1996; Meyer, 1999) may influence the seeding mechanisms for EPB formation. The role of planetary waves other than the Q6DW also remain to be investigated. It also is unknown the extent to which the influence of planetary waves on the day-to-day variability of EPBs may be seasonally dependent. Since winds in the E-region are potentially more important around solstice (Liu, 2020), while the F-region winds may be more important during equinox (Richmond et al., 2015), the influence of planetary waves on the day-to-day variability of EPBs may be more pronounced during solstice conditions. The present study focused only on solstice conditions, and the seasonality of how planetary waves may impact EPBs thus remains unknown. The present study additionally demonstrates that whole atmosphere models are crucial tools for understanding the day-to-day variations in the upper atmosphere, including the formation of EPBs.

Acknowledgments

WACCM-X is part of the Community Earth System Model (CESM) and the source code is available at http://www.cesm.ucar.edu. This material is based upon work supported by the National Center for Atmospheric Research, which is a major facility sponsored by the U.S. National Science Foundation under Cooperative Agreement 1852977. NP acknowledges support from NASA Grants NNH17ZDA001N07 and NNH220B82A is acknowledged. AM is partly supported by NASA awards SPVKK1RC2MZ3. EA acknowledges NASA support 80NSSC22K0171 and 80NSSC21K1310.

Open Research

WACCMX is part of the Community Earth System Model (CESM) and the source code is available at https://github.com/ESCOMP/CESM (Danabasoglu et al., 2019). The WACCM-X simulation output is available at https://doi.org/10.5065/52xt-9074 (Pedatella, 2023).

References

Aa, E., Zhang, S.-R., Liu, G., Eastes, R. W., Wang, W., Karan, D. K., ... Derghazarian, S. (2023). Statistical analysis of equatorial plasma bubbles climatology and multi-day periodicity using gold observations. *Geophysical Research Letters*, *50*, e2023GL103510. Retrieved from `https://agupubs.onlinelibrary.wiley.com/doi/abs/10.1029/2023GL103510` (e2023GL103510 2023GL103510) doi: https://doi.org/10.1029/2023GL103510

Aa, E., Zou, S., Eastes, R., Karan, D. K., Zhang, S.-R., Erickson, P. J., & Coster, A. J. (2020). Coordinated ground-based and space-based observations of equatorial plasma bubbles. *Journal of Geophysical Research: Space Physics*, *125*, e2019JA027569. Retrieved from `https://agupubs.onlinelibrary.wiley.com/doi/abs/10.1029/2019JA027569` (e2019JA027569 10.1029/2019JA027569) doi: https://doi.org/10.1029/2019JA027569

Abdu, M. A., Batista, I. S., Takahashi, H., MacDougall, J., Sobral, J. H., Medeiros,

A. F., & Trivedi, N. B. (2003). Magnetospheric disturbance induced equatorial plasma bubble development and dynamics: A case study in brazilian sector. *Journal of Geophysical Research: Space Physics*, *108*. doi: https://doi.org/10.1029/2002JA009721

Abdu, M. A., Batista, P. P., Batista, I. S., Brum, C. G. M., Carrasco, A. J., & Reinisch, B. W. (2006). Planetary wave oscillations in mesospheric winds, equatorial evening prereversal electric field and spread f. *Geophysical Research Letters*, *33*. doi: https://doi.org/10.1029/2005GL024837

Abdu, M. A., Brum, C. G. M., Batista, P. P., Gurubaran, S., Pancheva, D., Bageston, J. V., ... Takahashi, H. (2015). Fast and ultrafast kelvin wave modulations of the equatorial evening f region vertical drift and spread f development. *Earth, Planets and Space*, *67*, 1. doi: 10.1186/s40623-014-0143-5

Abdu, M. A., Iyer, K. N., de Medeiros, R. T., Batista, I. S., & Sobral, J. H. A. (2006). Thermospheric meridional wind control of equatorial spread f and evening prereversal electric field. *Geophysical Research Letters*, *33*. doi: https://doi.org/10.1029/2005GL024835

Abdu, M. A., Kherani, E. A., Batista, I. S., de Paula, E. R., Fritts, D. C., & Sobral, J. H. A. (2009). Gravity wave initiation of equatorial spread f/plasma bubble irregularities based on observational data from the spreadfex campaign. *Annales Geophysicae*, *27*, 2607-2622. doi: 10.5194/angeo-27-2607-2009

Abdu, M. A., Kherani, E. A., Batista, I. S., & Sobral, J. H. A. (2009). Equatorial evening prereversal vertical drift and spread f suppression by disturbance penetration electric fields. *Geophysical Research Letters*, *36*. doi: https://doi.org/10.1029/2009GL039919

Abdu, M. A., Ramkumar, T. K., Batista, I. S., Brum, C. G. M., Takahashi, H., Reinisch, B. W., & Sobral, J. H. A. (2006). Planetary wave signatures in the equatorial atmosphere–ionosphere system, and mesosphere- e- and f- region coupling. *Journal of Atmospheric and Solar-Terrestrial Physics*, *68*, 509-522. (Vertical Coupling in the Atmosphere/Ionosphere System) doi: https://doi.org/10.1016/j.jastp.2005.03.019

Burke, W. J., Gentile, L. C., Huang, C. Y., Valladares, C. E., & Su, S. Y. (2004). Longitudinal variability of equatorial plasma bubbles observed by dmsp and rocsat-1. *Journal of Geophysical Research: Space Physics*, *109*. doi: https://doi.org/10.1029/2004JA010583

Carter, B. A., Yizengaw, E., Retterer, J. M., Francis, M., Terkildsen, M., Marshall, R., ... Zhang, K. (2014). An analysis of the quiet time day-to-day variability in the formation of postsunset equatorial plasma bubbles in the southeast asian region. *Journal of Geophysical Research: Space Physics*, *119*, 3206-3223. doi: https://doi.org/10.1002/2013JA019570

Danabasoglu, Lamarque, Bacmeister, Bailey, DuVivier, Edwards, ... Strand (2019, 7). *Cesm-release-cesm2.1.1 [software].* Zenodo. Retrieved from `https://doi.org/10.5281/zenodo.3895315` doi: 10.5281/zenodo.3895315

Eastes, R. W., McClintock, W. E., Burns, A. G., Anderson, D. N., Andersson, L., Aryal, S., ... Woods, T. N. (2020). Initial observations by the gold mission. *Journal of Geophysical Research: Space Physics*, *125*, e2020JA027823. (e2020JA027823 2020JA027823) doi: https://doi.org/10.1029/2020JA027823

Eastes, R. W., McClintock, W. E., Burns, A. G., Anderson, D. N., Andersson, L., Codrescu, M., ... Oberheide, J. (2017). The global-scale observations of the limb and disk (gold) mission. *Space Science Reviews*, *212*, 383-408. doi: 10.1007/s11214-017-0392-2

Eastes, R. W., Solomon, S. C., Daniell, R. E., Anderson, D. N., Burns, A. G., England, S. L., ... McClintock, W. E. (2019). Global-scale observations of the equatorial ionization anomaly. *Geophysical Research Letters*, *46*, 9318-9326. doi: https://doi.org/10.1029/2019GL084199

Emery, B. A., Roble, R. G., Ridley, E. C., Richmond, A. D., Knipp, D. J., Crowley, G., . . . Maeda, S. (2012). Parameterization of the ion convection and the auroral oval in the ncar thermospheric general circulation models. *University Corporation for Atmospheric Research Technical Report*, *No. NCAR/T*. doi: 10.5065/D6N29TXZ

Fejer, B. G., & Kelley, M. C. (1980). Ionospheric irregularities. *Reviews of Geophysics*, *18*, 401-454. doi: https://doi.org/10.1029/RG018i002p00401

Fejer, B. G., Scherliess, L., & de Paula, E. R. (1999). Effects of the vertical plasma drift velocity on the generation and evolution of equatorial spread f. *Journal of Geophysical Research: Space Physics*, *104*, 19859-19869. doi: https://doi.org/10.1029/1999JA900271

Fesen, C. G., Crowley, G., Roble, R. G., Richmond, A. D., & Fejer, B. G. (2000). Simulation of the pre-reversal enhancement in the low latitude vertical ion drifts. *Geophysical Research Letters*, *27*, 1851-1854. doi: 10.1029/2000GL000061

Forbes, J. M., Maute, A., Zhang, X., & Hagan, M. E. (2018). Oscillation of the ionosphere at planetary-wave periods. *Journal of Geophysical Research: Space Physics*, *123*, 7634-7649. Retrieved from `https://agupubs.onlinelibrary.wiley.com/doi/abs/10.1029/2018JA025720` doi: https://doi.org/10.1029/2018JA025720

Forbes, J. M., Zhang, X., Heelis, R., Stoneback, R., Englert, C. R., Harlander, J. M., . . . Immel, T. J. (2021). Atmosphere-ionosphere (a-i) coupling as viewed by icon: Day-to-day variability due to planetary wave (pw)-tide interactions. *Journal of Geophysical Research: Space Physics*, *126*, e2020JA028927. (e2020JA028927 2020JA028927) doi: https://doi.org/10.1029/2020JA028927

Forbes, J. M., Zhang, X., Maute, A., & Hagan, M. E. (2018). Zonally symmetric oscillations of the thermosphere at planetary wave periods. *Journal of Geophysical Research: Space Physics*, *123*, 4110-4128. doi: https://doi.org/10.1002/2018JA025258

Gan, Q., Oberheide, J., & Pedatella, N. M. (2018). Sources, sinks, and propagation characteristics of the quasi 6-day wave and its impact on the residual mean circulation. *Journal of Geophysical Research: Atmospheres*, *123*, 9152-9170. doi: https://doi.org/10.1029/2018JD028553

Gan, Q., Oberheide, J., Yue, J., & Wang, W. (2017). Short-term variability in the ionosphere due to the nonlinear interaction between the 6 day wave and migrating tides. *Journal of Geophysical Research: Space Physics*, *122*, 8831-8846. doi: https://doi.org/10.1002/2017JA023947

Gasperini, F., Forbes, J. M., Doornbos, E. N., & Bruinsma, S. L. (2015). Wave coupling between the lower and middle thermosphere as viewed from timed and goce. *Journal of Geophysical Research: Space Physics*, *120*, 5788-5804. doi: https://doi.org/10.1002/2015JA021300

Gelaro, R., McCarty, W., Suárez, M. J., Todling, R., Molod, A., Takacs, L., . . . Zhao, B. (2017). The modern-era retrospective analysis for research and applications, version 2 (merra-2). *Journal of Climate*, *30*, 5419-5454. doi: 10.1175/JCLI-D-16-0758.1

Gentile, L. C., Burke, W. J., & Rich, F. J. (2006). A climatology of equatorial plasma bubbles from dmsp 1989–2004. *Radio Science*, *41*. doi: https://doi.org/10.1029/2005RS003340

Ghosh, P., Otsuka, Y., Mani, S., & Shinagawa, H. (2020). Day-to-day variation of pre-reversal enhancement in the equatorial ionosphere based on gaia model simulations. *Earth, Planets and Space*, *72*, 93. doi: 10.1186/s40623-020-01228-9

Gu, S.-Y., Liu, H.-L., Dou, X., & Jia, M. (2018). Ionospheric variability due to tides and quasi-two day wave interactions. *Journal of Geophysical Research: Space Physics*, *123*, 1554-1565. doi: https://doi.org/10.1002/2017JA025105

Heelis, R. A., Lowell, J. K., & Spiro, R. W. (1982). A model of the high-latitude ionospheric convection pattern. *Journal of Geophysical Research: Space Physics*, *87*, 6339-6345. doi: 10.1029/JA087iA08p06339

Huang, C.-S., & Hairston, M. R. (2015). The postsunset vertical plasma drift and its effects on the generation of equatorial plasma bubbles observed by the c/nofs satellite. *Journal of Geophysical Research: Space Physics*, *120*, 2263-2275. doi: https://doi.org/10.1002/2014JA020735

Huba, J. D. (2021). Theory and modeling of equatorial spread f. In (p. 185-200). American Geophysical Union (AGU). doi: https://doi.org/10.1002/9781119815617.ch10

Huba, J. D., & Krall, J. (2013). Impact of meridional winds on equatorial spread f: Revisited. *Geophysical Research Letters*, *40*, 1268-1272. doi: https://doi.org/10.1002/grl.50292

Huba, J. D., Krall, J., & Drob, D. (2020). Modeling the impact of metallic ion layers on equatorial spread with sami3/esf. *Geophysical Research Letters*, *47*, e2020GL087224. (e2020GL087224 10.1029/2020GL087224) doi: https://doi.org/10.1029/2020GL087224

Huba, J. D., & Liu, H.-L. (2020). Global modeling of equatorial spread f with sami3/waccm-x. *Geophysical Research Letters*, *47*, e2020GL088258. Retrieved from `https://agupubs.onlinelibrary.wiley.com/doi/abs/10.1029/2020GL088258` doi: https://doi.org/10.1029/2020GL088258

Hysell, D. L. (2000). An overview and synthesis of plasma irregularities in equatorial spread f. *Journal of Atmospheric and Solar-Terrestrial Physics*, *62*, 1037-1056. doi: https://doi.org/10.1016/S1364-6826(00)00095-X

Karan, D. K., Daniell, R. E., England, S. L., Martinis, C. R., Eastes, R. W., Burns, A. G., & McClintock, W. E. (2020). First zonal drift velocity measurement of equatorial plasma bubbles (epbs) from a geostationary orbit using gold data. *Journal of Geophysical Research: Space Physics*, *125*, e2020JA028173. (e2020JA028173 2020JA028173) doi: https://doi.org/10.1029/2020JA028173

Karan, D. K., Eastes, R. W., Daniell, R. E., Martinis, C. R., & McClintock, W. E. (2023). Gold mission's observation about the geomagnetic storm effects on the nighttime equatorial ionization anomaly (eia) and equatorial plasma bubbles (epb) during a solar minimum equinox. *Space Weather*, *21*, e2022SW003321. (e2022SW003321 2022SW003321) doi: https://doi.org/10.1029/2022SW003321

Kelley, M. C., Makela, J. J., de La Beaujardière, O., & Retterer, J. (2011). Convective ionospheric storms: A review. *Reviews of Geophysics*, *49*. doi: https://doi.org/10.1029/2010RG000340

Kil, H., Paxton, L. J., & Oh, S.-J. (2009). Global bubble distribution seen from rocsat-1 and its association with the evening prereversal enhancement. *Journal of Geophysical Research: Space Physics*, *114*. doi: https://doi.org/10.1029/2008JA013672

Lieberman, R. S., Riggin, D. M., Franke, S. J., Manson, A. H., Meek, C., Nakamura, T., … Reid, I. (2003). The 6.5-day wave in the mesosphere and lower thermosphere: Evidence for baroclinic/barotropic instability. *Journal of Geophysical Research: Atmospheres*, *108*. doi: 10.1029/2002JD003349

Liu, H.-L. (2020). Day-to-day variability of prereversal enhancement in the vertical ion drift in response to large-scale forcing from the lower atmosphere. *Space Weather*, *18*, e2019SW002334. Retrieved from `https://agupubs.onlinelibrary.wiley.com/doi/abs/10.1029/2019SW002334` doi: https://doi.org/10.1029/2019SW002334

Liu, H.-L., Bardeen, C. G., Foster, B. T., Lauritzen, P., Liu, J., Lu, G., … Wang, W. (2018). Development and validation of the whole atmosphere community climate model with thermosphere and ionosphere extension (waccm-x 2.0). *Journal of Advances in Modeling Earth Systems*, *10*, 381-402. doi: 10.1002/2017MS001232

Liu, H.-L., & Richmond, A. D. (2013). Attribution of ionospheric vertical plasma drift perturbations to large-scale waves and the dependence on solar activity. *Journal of Geophysical Research: Space Physics*, *118*, 2452-2465. doi: 10.1002/jgra.50265

Liu, H.-L., Talaat, E. R., Roble, R. G., Lieberman, R. S., Riggin, D. M., & Yee, J.-H. (2004). The 6.5-day wave and its seasonal variability in the middle and upper atmosphere. *Journal of Geophysical Research: Atmospheres*, *109*. doi: 10.1029/2004JD004795

Liu, H.-L., Wang, W., Richmond, A. D., & Roble, R. G. (2010). Ionospheric variability due to planetary waves and tides for solar minimum conditions. *Journal of Geophysical Research: Space Physics*, *115*. doi: https://doi.org/10.1029/2009JA015188

Makela, J. J., & Miller, E. S. (2008). Optical observations of the growth and day-to-day variability of equatorial plasma bubbles. *Journal of Geophysical Research: Space Physics*, *113*. doi: https://doi.org/10.1029/2007JA012661

Martinis, C., Daniell, R., Eastes, R., Norrell, J., Smith, J., Klenzing, J., ... Burns, A. (2021). Longitudinal variation of postsunset plasma depletions from the global-scale observations of the limb and disk (gold) mission. *Journal of Geophysical Research: Space Physics*, *126*, e2020JA028510. (e2020JA028510 2020JA028510) doi: https://doi.org/10.1029/2020JA028510

McClintock, W. E., Eastes, R. W., Hoskins, A. C., Siegmund, O. H. W., McPhate, J. B., Krywonos, A., ... Burns, A. G. (2020). Global-scale observations of the limb and disk mission implementation: 1. instrument design and early flight performance. *Journal of Geophysical Research: Space Physics*, *125*, e2020JA027797. (e2020JA027797 2020JA027797) doi: https://doi.org/10.1029/2020JA027797

Meyer, C. K. (1999). Gravity wave interactions with mesospheric planetary waves: A mechanism for penetration into the thermosphere-ionosphere system. *Journal of Geophysical Research: Space Physics*, *104*, 28181-28196. doi: https://doi.org/10.1029/1999JA900346

Meyer, C. K., & Forbes, J. M. (1997). A 6.5-day westward propagating planetary wave: Origin and characteristics. *Journal of Geophysical Research: Atmospheres*, *102*, 26173-26178. doi: https://doi.org/10.1029/97JD01464

Miyoshi, Y., & Yamazaki, Y. (2020). Excitation mechanism of ionospheric 6-day oscillation during the 2019 september sudden stratospheric warming event. *Journal of Geophysical Research: Space Physics*, *125*, e2020JA028283. (e2020JA028283 2020JA028283) doi: https://doi.org/10.1029/2020JA028283

Pancheva, D., Haldoupis, C., Meek, C. E., Manson, A. H., & Mitchell, N. J. (2003). Evidence of a role for modulated atmospheric tides in the dependence of sporadic e layers on planetary waves. *Journal of Geophysical Research: Space Physics*, *108*. Retrieved from `https://agupubs.onlinelibrary.wiley.com/doi/abs/10.1029/2002JA009788` doi: https://doi.org/10.1029/2002JA009788

Pancheva, D., Merzlyakov, E., Mitchell, N. J., Portnyagin, Y., Manson, A. H., Jacobi, C., ... Oleynikov, A. N. (2002). Global-scale tidal variability during the psmos campaign of june–august 1999: interaction with planetary waves. *Journal of Atmospheric and Solar-Terrestrial Physics*, *64*, 1865-1896. doi: https://doi.org/10.1016/S1364-6826(02)00199-2

Pedatella, N. M. (2023). *Waccm-x simulations for november 2020 to december 2021.* UCAR/NCAR - GDEX. Retrieved from `https://doi.org/10.5065/52xt-9074` doi: 10.5065/52xt-9074

Pedatella, N. M., Liu, H.-L., & Hagan, M. E. (2012). Day-to-day migrating and nonmigrating tidal variability due to the six-day planetary wave. *Journal of Geophysical Research: Space Physics*, *117*. doi: https://doi.org/10.1029/2012JA017581

Ram, S. T., Rao, P. V. S. R., Prasad, D. S. V. V. D., Niranjan, K., Krishna, S. G., Sridharan, R., & Ravindran, S. (2008). Local time dependent response of postsunset esf during geomagnetic storms. *Journal of Geophysical Research: Space Physics*, *113*. doi: https://doi.org/10.1029/2007JA012922

Richmond, A. D., Fang, T.-W., & Maute, A. (2015). Electrodynamics of the equatorial evening ionosphere: 1. importance of winds in different regions. *Journal of Geophysical Research: Space Physics*, *120*, 2118-2132. Retrieved from `https://agupubs.onlinelibrary.wiley.com/doi/abs/10.1002/2014JA020934` doi: https://doi.org/10.1002/2014JA020934

Smith, A. K. (1996). Longitudinal variations in mesospheric winds: Evidence for gravity wave filtering by planetary waves. *Journal of Atmospheric Sciences*, *53*, 1156-1173. doi: https://doi.org/10.1175/1520-0469(1996)053⟨1156:LVIMWE⟩2.0.CO;2

Smith, A. K., Pedatella, N. M., Marsh, D. R., & Matsuo, T. (2017). On the dynamical control of the mesosphere–lower thermosphere by the lower and middle atmosphere. *Journal of the Atmospheric Sciences*, *74*, 933-947. doi: 10.1175/JAS-D-16-0226.1

Solomon, S. C., & Qian, L. (2005). Solar extreme-ultraviolet irradiance for general circulation models. *Journal of Geophysical Research: Space Physics*, *110*. doi: https://doi.org/10.1029/2005JA011160

Stephan, A. W., Colerico, M., Mendillo, M., Reinisch, B. W., & Anderson, D. (2002). Suppression of equatorial spread f by sporadic e. *Journal of Geophysical Research: Space Physics*, *107*, SIA 4-1-SIA 4-5. doi: https://doi.org/10.1029/2001JA000162

Su, S.-Y., Chao, C. K., & Liu, C. H. (2008). On monthly/seasonal/longitudinal variations of equatorial irregularity occurrences and their relationship with the postsunset vertical drift velocities. *Journal of Geophysical Research: Space Physics*, *113*. doi: https://doi.org/10.1029/2007JA012809

Sultan, P. J. (1996). Linear theory and modeling of the rayleigh-taylor instability leading to the occurrence of equatorial spread f. *Journal of Geophysical Research: Space Physics*, *101*, 26875-26891. doi: https://doi.org/10.1029/96JA00682

Talaat, E. R., Yee, J.-H., & Zhu, X. (2002). The 6.5-day wave in the tropical stratosphere and mesosphere. *Journal of Geophysical Research: Atmospheres*, *107*, ACL 1-1-ACL 1-5. doi: https://doi.org/10.1029/2001JD000822

Teitelbaum, H., & Vial, F. (1991). On tidal variability induced by nonlinear interaction with planetary waves. *Journal of Geophysical Research: Space Physics*, *96*, 14169-14178. doi: 10.1029/91JA01019

Tsunoda, R. T. (1985). Control of the seasonal and longitudinal occurrence of equatorial scintillations by the longitudinal gradient in integrated e region pedersen conductivity. *Journal of Geophysical Research: Space Physics*, *90*, 447-456. Retrieved from `https://agupubs.onlinelibrary.wiley.com/doi/abs/10.1029/JA090iA01p00447` doi: https://doi.org/10.1029/JA090iA01p00447

Tsunoda, R. T. (2007). Seeding of equatorial plasma bubbles with electric fields from an es-layer instability. *Journal of Geophysical Research: Space Physics*, *112*. doi: https://doi.org/10.1029/2006JA012103

Wu, D. L., Hays, P. B., & Skinner, W. R. (1994). Observations of the 5-day wave in the mesosphere and lower thermosphere. *Geophysical Research Letters*, *21*, 2733-2736. doi: https://doi.org/10.1029/94GL02660

Wu, Q. (2015). Longitudinal and seasonal variation of the equatorial flux tube integrated rayleigh-taylor instability growth rate. *Journal of Geophysical Research: Space Physics*, *120*, 7952-7957. doi: https://doi.org/10.1002/2015JA021553

Yamazaki, Y., & Diéval, C. (2021). Modeling of planetary wave influences on the pre-reversal enhancement of the equatorial f region vertical plasma drift. *Space Weather*, *19*, e2020SW002685. (e2020SW002685 2020SW002685) doi: https://

doi.org/10.1029/2020SW002685

Yokoyama, T. (2017). A review on the numerical simulation of equatorial plasma bubbles toward scintillation evaluation and forecasting. *Progress in Earth and Planetary Science*, *4*, 37. doi: 10.1186/s40645-017-0153-6

Yue, J., Wang, W., Ruan, H., Chang, L. C., & Lei, J. (2016). Impact of the interaction between the quasi-2 day wave and tides on the ionosphere and thermosphere. *Journal of Geophysical Research: Space Physics*, *121*, 3555-3563. doi: https://doi.org/10.1002/2016JA022444